

# Synthesis, Characterization and Application of Strontium Doped Zinc Ferrite Nanomaterials

Milind (Physics), Researcher, Sunrise University, Alwar (Raj.)  
Dr. Vipin Kumar (Physics), Professor, Sunrise University, Alwar (Raj.)

## Abstract

*Strontium-doped zinc ferrite nanoparticles (Sr-ZnFe<sub>2</sub>O<sub>4</sub>) were synthesized using a sol-gel self-ignition method and characterized by PXRD, FTIR, FESEM, EDX, VSM, and UV-Visible spectroscopy. The particles exhibited a cubic spinel ferrite phase, with changes in crystallite size and lattice constant upon strontium doping. FTIR confirmed water and hydroxyl groups. Sr<sub>0.2</sub>Zn<sub>0.8</sub>Fe<sub>2</sub>O<sub>4</sub> nanoparticles demonstrated promising performance as thin-film humidity sensors, with high sensitivity,*

**Keywords:** *Strontium-doped zinc ferrite nanoparticles, Thin –film humidity sensors*

## INTRODUCTION

It is generally acknowledged that the properties of nanoparticles differ significantly from those of their bulk equivalents. The primary reason for this is the nanoscale dimensions of the materials [Khirade et al., 2020]. These dimensions give rise to a greater proportion of atoms at the surface, a greater ratio of surface area to volume, the quantum confinement effect, spatial confinement, and a reduced presence of defects. Size effects endow nanomaterials with an extraordinary and intriguing characteristic. Magnetic nanomaterial distinguishes itself from other nanomaterials as a prospective candidate for a diverse range of applications on account of its enhanced configuration and magnetic characteristics. Ferrites nanoparticles are the preeminent constituents of the magnetic material family on account of their exceptional characteristics and adaptability across diverse domains, including but not limited to gas sensing, magnetic hyperthermia, drug delivery, and memory storage. Due to the fact that the properties of spinel structures and, consequently, their applications are readily modifiable, their underlying physics remains fascinating. Recent research has revealed that by altering the physical properties of these materials, novel opportunities have emerged, prompting the investigation of various avenues of inquiry [Ali et al., 2020]. The typical chemical formula for spinel ferrites is MFe<sub>2</sub>O<sub>4</sub>, where M denotes a divalent cation. The oxygen atoms comprise the face-centered cubic lattice structure of the spinel ferrites. This FCC structure is composed of octahedral and tetrahedral sublattices. Divalent and trivalent cation occupation at distinct lattice sites lend spinel its varied nomenclature. A substance is classified as "normal spinel" when its divalent elements occupy a tetrahedral site. Conversely, spinel ferrite at an octahedral orientation is referred to as an inverse spinel ferrite. Mixed spinel refers to a material in which atoms, specifically divalent and trivalent cations, are arbitrarily distributed on both sites in between these two. The manner in which cations are distributed across various lattice sites in spinel ferrite significantly affects its magnetic and electrical properties, among others. Gas sensors, computer memory processors, transformer cores, ferrofluids, recording media, microwave devices, spintronics, magnetic refrigeration, catalysis, and biosensors all make use of spinel ferrites [Nadeem et al., 2015; Shoba et al., 2020]. As a basal material, this chapter is limited to zinc ferrite nanomaterial. Zinc ferrites, owing to their flexible ferrite nature and minimal toxicity, have emerged as the most promising substance for biomedical implementations. In recent decades, the industrial and medical applications of zinc ferrite nanoparticles have increased dramatically [Andhare et al., 2020]. The research examined in this chapter focuses specifically on nanomaterials composed of zinc ferrite (ZnFe<sub>2</sub>O<sub>4</sub>) doped with strontium (Sr). This article provides a concise summary of the research conducted in recent years regarding strontium-doped zinc ferrite.

In their study, Shoba et al. (2020) utilized the co-precipitation method to synthesize zinc ferrite doped with strontium (ZnFe<sub>2-x</sub>Sr<sub>x</sub>O). The authors observed that the magnetization, band gap, and dielectric constant all increased in accordance with the strontium content. In their hydrothermal synthesis of strontium-doped zinc ferrite, Amutha et al. discovered that as the quantity of strontium increases, the lattice parameter rises while the crystallite size decreases [Amutha et al., 2020]. In their study, Manikandan et al. (2013) synthesized strontium-doped zinc ferrite nanomaterial via microwave combustion. The authors characterized the resulting

sample as ferromagnetic at high strontium concentrations but superparamagnetic at low concentrations (0.2). A correlation was observed between strontium concentration and an increase in the band gap, as reported by Tholkappian et al. (2015). It is evident from the aforementioned literature reviews that research on strontium-doped zinc ferrite nanomaterials is limited. To the author's knowledge, there are no published reports on the utilization of this composition for humidity sensing, despite the notable sensitivity of spinel ferrites to humidity. An essential characteristic of ferrites is their porosity, a fundamental requirement for the development of a humidity sensor. Additionally, the resistance of the ferrite compositions is quite high, but it can decrease as the relative humidity increases [Rezlescu et al., 2005]. The presence of a multitude of perforations on the surface of the spinel ferrite nanomaterial promotes the absorption and condensation of water vapor. Additionally, it is noted that alkaline earth atoms exhibit a robust attraction towards water molecules. The author's investigation into the synthesis, analysis, and application of Sr-doped  $ZnFe_2O_4$  nanoparticles as humidity sensors was prompted by these particulars.

Humidity is a critical and essential environmental factor for industries, medical services, agriculture, and more. Humidity measurement is critical in numerous scientific and technological disciplines and plays a substantial role in averting the transmission of viruses and other pathogens [Rahman et al., 2022]. The gaseous state of water is commonly referred to as humidity. Relative humidity (RH), a prevalent descriptor for humidity, is measured in percentage (% RH) [Farahani et al., 2014]. Water vapor is converted to an electrical signal by a humidity sensor, which is then output as impedance, capacitance, and so forth. The meteorology, aerospace exploration, medical equipment, environmental protection, robotics, automotive, and semiconductor industries all utilize humidity sensors [Arunachalam et al., 2019; Tripathy et al., 2014; Pi et al., 2021; Zhu et al., 2020; Liu et al., 2017]. In recent times, significant progress has been made in the development of humidity sensors, which has opened up intriguing prospects for their implementation in noncontact sensing, soft robotics, health monitoring, and even the real-time monitoring of human respiration rates. By utilizing a humidity sensor array for non-contact sensing and contactless interface localization applications, the risk of bacterial transmission associated with conventional touch displays can be reduced [Trunget al., 2017; Zhao et al., 2017; Liet al., 2017; Wu et al., 2019; Wang et al., 2021]. For the controlled monitoring, regulation, and management of humidity, low response times, high sensitivity, chemical and thermal stability, and resistance to contaminants are essential [Tripathy et al., 2016]. Sensing elements include polymers, inorganic nanocomposites, 2D nanomaterials, and carbon-based nanomaterials [Kumar et al., 2020; Singh et al., 2021; Guo et al., 2018]. Sensitivity and close stability across a broad spectrum of humidity levels.

In 1938, Dunmore conducted humidity measurements using the initial LiCl-based electrolytic sensor he developed [Dunmore, 1938]. In their comprehensive investigation of absolute humidity sensors, Chen et al. (2005) also addressed the issue of stability-related parameters in the  $Al_2O_3$  moisture sensor. In their investigation, Jeseentharani et al. (2013) assessed the sensitivity of various metal ferrites to humidity and determined that zinc ferrite exhibits the highest level of sensitivity. Kumar et al. [Kumar et al., 2017] synthesized cobalt ferrite and investigated its humidity sensing properties; they concluded that the hexagonal configuration exhibited the greatest sensitivity. In their investigation of the capability of zinc ferrite nanomaterial to detect humidity, Nikolic et al. (2019) observed a nearly 46-fold reduction in impedance at a frequency of 42 hertz. As stated by Sathisha et al. (2020), the material that was synthesized exhibits remarkable stability when exposed to elevated temperatures. It further elucidates the humidity sensing characteristics of copper ferrite doped with bismuth. Shaheen et al. explored the moisture sensing characteristics of metal oxide composites in their study [Shaheen et al., 2020]. They discovered that their response and recuperation times are adequate and that they are more stable. In their study, El-Denglawey et al. (2021) synthesized Mn-Zn ferrites doped with dysprosium and noted a notable enhancement in these ferrites' behavior when exposed to humidity. Nikita et al. [Nitika et al., 2021] synthesized the zinc ferrite

nanoparticles and investigated the material's ability to detect humidity; they discovered that it exhibited exceptional humidity sensitivity at 700°C.

Utilizing the sol-gel autocombustion method, this research endeavors to produce  $\text{Sr}_x\text{Zn}_{1-x}\text{Fe}_2\text{O}_4$  with  $x$  values of 0.0, 0.05, 0.10, 0.15, 0.20, 0.25, and 0.30. Additionally, this study seeks to assess the material's viability as a precursor to thin film humidity sensors. Using powder XRD, the phase identification and crystal structure were ascertained. To investigate surface morphology, functional groups, and constituent elements, EDX, FTIR, and FESEM characterization techniques were implemented. The magnetic and optical properties were investigated utilizing a VSM and UV-Visible spectrophotometer, in that order. By employing the nanomaterial that was synthesized, a thin-film humidity sensor has been engineered. Multiple facets of the humidity sensor that was developed have been the subject of an investigation.

## EXPERIMENT

### Production of Zinc Ferrite Doped with Strontium

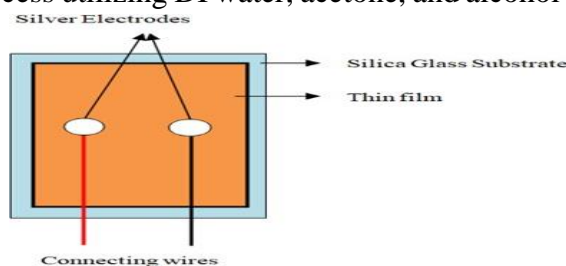
The zinc ferrite nanomaterial enriched with strontium is synthesized via sol-gel autocombustion. The procedure utilizes the following reagents: strontium nitrate ( $\text{Sr}(\text{NO}_3)_2$ ), ferric nitrate ( $\text{Fe}(\text{NO}_3)_3 \cdot 9\text{H}_2\text{O}$ ) at 98.5% purity, zinc nitrate ( $\text{Zn}(\text{NO}_3)_2 \cdot 6\text{H}_2\text{O}$ ) at 99% purity, and citric acid at 99.8% purity, all of which were procured from Merk India, Fisher Scientific, Alfa Aesar, and Fizmerk India, respectively. A homogeneous solution was produced by dissolving these compounds in 100 mL of DI water at the correct stoichiometry ratio. In order to regulate the pH of the solution to 7, ammonia was introduced drop by drop while the mixture was subjected to continuous heating at 80 °C for fifty minutes. The reaction mixture was subsequently heated at 235 °C for an additional three hours using a hot plate. The solution has begun to solidify into a gel at this juncture; it will eventually ignite spontaneously and reduce to charcoal. After cooling to room temperature, this ash was pulverized into a powder using a mortar and pestle. The fine material underwent a calcination process at 800 °C for a duration of five hours. In order to conduct additional research, this calcined material was utilized.

## CHARACTERIZATIONS

The crystal phase and structural properties of the pulverized materials that were synthesized were investigated using an X-ray diffractometer (Bruker Model-08 Advance, Eco) at a temperature of 25°C and an angle of 10–80°. Two electrons per minute was the scan rate utilized to acquire the XRD spectra. The investigation of particulate size, shape, and distribution was facilitated through the utilization of FESEM (JEOL JSM 7610F plus). An EDX (Octane Eleit by AMETEK) conducted at 15 kV to 20 kV provides confirmation of the composition of elements. The KBr standard was utilized to generate the infrared spectra, which were obtained with an FTIR spectrometer (Spectrum Two, Perkin Elmer) and a  $1 \text{ cm}^{-1}$  resolution between 4000 and  $375 \text{ cm}^{-1}$ . The VSM (Two Tesla Cryogen-free VSM, Quantum Design Inc.) was utilized to investigate the magnetic properties, while the UV Visible spectrophotometer (Baise UV Visible spectrometer, Evaluation 201 Theromscientific) was employed to measure optical bands.

### Design of sensing material and humidity measurement

The humidity sensing investigation involves the fabrication of the sensing element through the application of a thin film of synthesized nanomaterial onto a silica glass substrate. Following a thorough cleansing process utilizing DI water, acetone, and alcohol (isopropyl),  $1.0 \times 1.0 \text{ cm}^2$



silica glass substrates were subjected to sonication for a duration of 30 minutes. Ten minutes are spent in an oven preheated to dry the substrates. Dissolving the synthesized substance in distilled water results in the formation of a homogeneous solution. A slender film is formed by

applying a minute amount of this solution via a spin coater (rpm 1500) housed in a vacuum chamber onto a pristine glass substrate. To cure the thin film, it is heated at 60 degrees Celsius for 30 minutes on a hot plate. To assure proper fixing, the film is annealed at 450°C for two hours in an atmosphere containing 20% oxygen. For electrode growth, silver paste is utilized [Gupta et al., 2021]. As a sensing material, the manufactured thin film is utilized for additional research. The humidity sensitivity is evaluated using a glass chamber containing controlled humidity via a petri dish and a hygrometer, as depicted in the symbolic diagram of the sensing material in Figure 1. To control the relative humidity within the glass chamber, saturated solutions of potassium sulphate and potassium hydroxide in water are retained for the purposes of humidification and dehumidification. In order to determine impedance, electrodes are linked to wire using an LCR meter (Wayne Kerr, 6440B) [Tiwari et al., 2022, Priya et al., 2021]. as depicted in Figure 2. The data was collected at ambient temperature and a frequency of 100 hertz.

**Fig.1: Sensing Element**

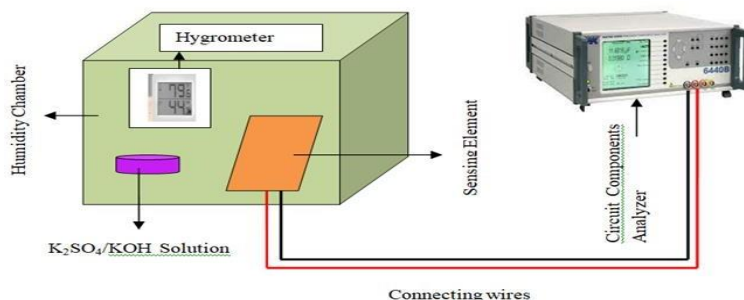


**Fig.2: Experimental setup for Humidity Sensing Measurement**

**RESULTS AND DISCUSSION**

**Powder X-ray diffraction (PXRD) analysis**

PXRD was used to analyze the produced nanomaterial for phase identification and crystal structure. The X-ray diffractogram at room temperature for all  $Sr_xZn_{1-x}Fe_2O_4$  compositions ( $x = 0.0, 0.05, 0.10, 0.15, 0.25, \text{ and } 0.3$ ) is displayed in Fig. 3. The cubic spinel ferrite phase with space group  $Fd3m$  is denoted by the sharp and intense peaks, displaying the diffraction patterns from planes (111), (220), (311), (222), (400), (422), (511), (440), and (533).  $ZnFe_2O_4$ 's diffraction peak angle values were compared to those listed on JCPDS card 22-1012 [Manikandan et al., 2013]. As Sr is doped into a material, two impurity phases— $\bullet Sr_2FeO_4$  and  $*SrFe_{12}O_{19}$ —appear in the spectra [Mazumdar et al., 2019, Li et al., 2016]. These secondary phases are likewise seen to become more prominent when Sr concentrations rise. According to the following relations [Kuru et al., 2020], the average crystallite size (D) and the plane lattice parameters (a) can be determined from the strongest intensity peak corresponding to (311).

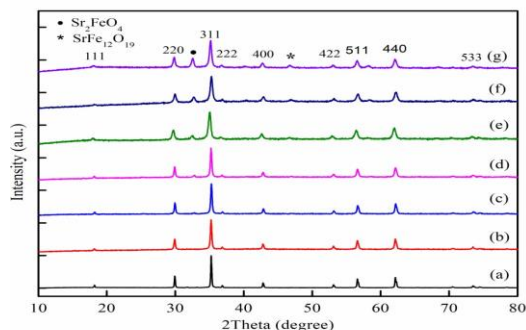


**Fig. 3: PXRD diffraction pattern of  $Sr_xZn_{(1-x)}Fe_2O_4$  (a)  $x=0$ , (b)  $x=0.05$ , (c)  $x=0.10$ , (d)  $x=0.15$ , (e)  $x=0.20$ , (f)  $x=0.25$ , (g)  $x=0.30$**

The lattice constant (a) is given by

$$a = \frac{\lambda \sqrt{h^2+k^2+l^2}}{2 \sin\theta}$$

.....(1)where,  $\lambda$  is wavelength of X-ray radiation used during the measurement, h, k, l are Miller indices,  $\theta$  is Bragg's angle.

$$D = \frac{0.9 \lambda}{\beta \cos \theta} \dots\dots\dots(2)$$

where,  $\beta$  is the value of FWHM for the intense peak (311) and  $\theta$  is Bragg's angle  
 The following equations are used to determine the nanomaterial's unit cell volume, X-ray density, and porosity [Kuru et al., 2020].

$$\text{The volume of unit cell is given by } V = a^3 \dots\dots\dots(3)$$

The X- ray density is given as

$$d_x = \frac{8M}{Na^3} \dots\dots\dots(4)$$

where M and N are molecular weight and Avogadro number respectively.

The Porosity is defined as

$$P = \left(1 - \frac{d_b}{d_x}\right) \times 100 \dots\dots(5)$$

where  $d_b$  and  $d_x$  are bulk density and X- ray density.

**Table 1: Structural parameters of Sr doped zinc ferrite nanomaterials**

Composition	Crystallite size (D) in nm	Interplanar distance (dhkl) Å	Lattice parameter (a) in Å	Volume (V) in Å <sup>3</sup>	X-ray density (dx) gm/cm <sup>3</sup>	Porosity (%)
ZnFe <sub>2</sub> O <sub>4</sub>	50.350	2.5454	8.442	601.1	5.328381	7.897
Sr <sub>0.05</sub> Zn <sub>0.95</sub> Fe <sub>2</sub> O <sub>4</sub>	40.814	2.5461	8.444	602.1	5.343421	12.842
Sr <sub>0.10</sub> Zn <sub>0.90</sub> Fe <sub>2</sub> O <sub>4</sub>	37.620	2.5461	8.445	602.1	5.365845	8.429
Sr <sub>0.15</sub> Zn <sub>0.85</sub> Fe <sub>2</sub> O <sub>4</sub>	36.426	2.5464	8.446	602.4	5.388591	5.015
Sr <sub>0.20</sub> Zn <sub>0.80</sub> Fe <sub>2</sub> O <sub>4</sub>	30.340	2.5468	8.446	602.6	5.413075	11.277
Sr <sub>0.25</sub> Zn <sub>0.85</sub> Fe <sub>2</sub> O <sub>4</sub>	28.935	2.5469	8.447	602.7	5.435516	22.262
Sr <sub>0.30</sub> Zn <sub>0.70</sub> Fe <sub>2</sub> O <sub>4</sub>	28.330	2.5475	8.449	603.1	5.456215	16.543

According to Table 1, as Sr increases, the lattice constant (a) rises and the crystallite size (D) falls. The increase in lattice constant is due to differences in ionic radii [Manikandan et al., 2013] between Sr<sup>2+</sup> (1.44), Zn<sup>2+</sup> (0.83), and Fe<sup>3+</sup> (0.64). By exchanging the tiny Zn<sup>2+</sup> or Fe<sup>3+</sup> particles for the larger Sr<sup>2+</sup> ions, the lattice can accommodate more atoms. This form of lattice growth induces strain, which in turn promotes interstress, which ultimately impedes grain development. Sr<sup>2+</sup> ions are segregated from the spinel structure and collected at the grain boundary as secondary phases of Sr<sub>2</sub>FeO<sub>4</sub> and SrFe<sub>12</sub>O<sub>19</sub> [Li et al., 2016], causing the crystallite size to decrease. Humidity is typically measured by observing how water molecules react to a synthetic material's surface. The surface contact process relies heavily on the granule's pore size and permeability. The produced nanomaterial is suitable for studies involving humidity sensing, as indicated by the computed porosity values.

**FTIR Spectroscopy**

The presence of functional groups in a material can be determined using FTIR spectroscopy

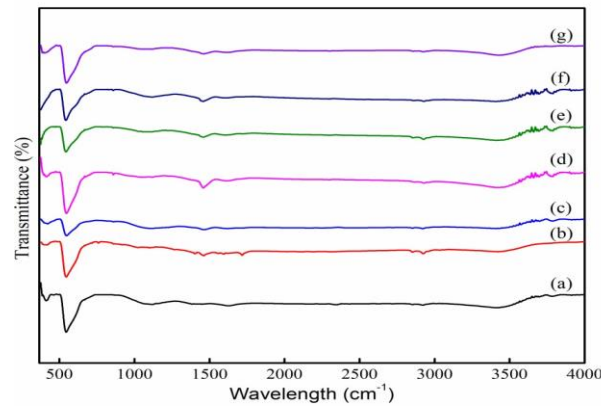


**Fig. 4: FTIR spectra of  $Sr_xZn(1-x)Fe_2O_4$ (a)  $x=0$ , (b)  $x=0.05$ , (c)  $x=0.10$ , (d)  $x=0.15$ , (e)  $x=0.20$ , (f)  $x=0.25$ , (g)  $x=0.30$**

In Fig. 4, we see the FTIR spectrum of the prepared sample recorded in the 4000-375  $cm^{-1}$  region. As can be seen in Fig. 5.4, the distinctive vibrational bands of zinc ferrite are the two strong bands (absorption) at wavelengths less than 700  $cm^{-1}$  [Shoba et al., 2020]. The vibration of metal and oxygen at octahedral and tetrahedral sites are reflected in the absorption bands presented in Table 5.2 with wavenumbers ( $v_1$ ) 379-410  $cm^{-1}$  and ( $v_2$ ) 545-542  $cm^{-1}$ . Bands ( $v_3$ ) in the vibrational spectrum at 1624  $cm^{-1}$  are associated with the stretched and bent vibrational modes of the H-O-H molecule. Similarly, the O-H bond vibration in free or absorbed  $H_2O$  molecules causes the vibrational bands ( $v_4$ ) at 3416  $cm^{-1}$ . These tremors signify that the manufactured nanomaterial is hygroscopic and convey the existence of both free and absorbed water. Having this property demonstrates that the produced nanomaterial can be put to use in studying humidity sensing.

**Table 2: Vibrational frequencies by FTIR spectroscopy**

Composition	Wavenumbers ( $cm^{-1}$ )			
	$v_1$	$v_2$	$v_3$	$v_4$
ZnFe <sub>2</sub> O <sub>4</sub>	396.34	545.78	1635.59	3443.62
Sr <sub>0.05</sub> Zn <sub>0.95</sub> Fe <sub>2</sub> O <sub>4</sub>	407.67	545.10	1623.74	3420.82
Sr <sub>0.10</sub> Zn <sub>0.90</sub> Fe <sub>2</sub> O <sub>4</sub>	410.82	544.31	1624.56	3421.92
Sr <sub>0.15</sub> Zn <sub>0.85</sub> Fe <sub>2</sub> O <sub>4</sub>	410.99	545.96	1618.58	3421.36
Sr <sub>0.20</sub> Zn <sub>0.80</sub> Fe <sub>2</sub> O <sub>4</sub>	400.01	542.80	1614.03	3421.92
Sr <sub>0.25</sub> Zn <sub>0.75</sub> Fe <sub>2</sub> O <sub>4</sub>	398.51	542.54	1610.01	3415.67
Sr <sub>0.30</sub> Zn <sub>0.70</sub> Fe <sub>2</sub> O <sub>4</sub>	397.35	542.64	1619.29	3436.84

### FESEM ANALYSIS

Fig. 5 displays the results of FESEM analysis of the microstructure and surface morphology of strontium-doped zinc ferrite nanoparticles. Particles appear almost spherical, clumped together due to their magnetic structure, and porous in the photos. The porous structure of the synthesized materials suggests that they could be used in a humidity sensor.

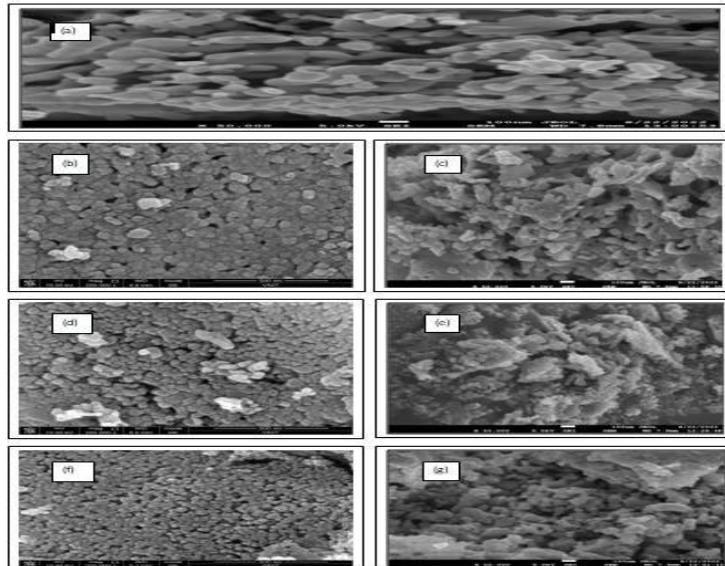


**Fig. 5: FESEM image  $Sr_xZn_{(1-x)}Fe_2O_4$  (a)  $x=0$ , (b)  $x=0.05$ , (c)  $x=0.10$ , (d)  $x=0.15$ , (e)  $x=0.20$ , (f)  $x=0.25$ , (g)  $x=0.30$**

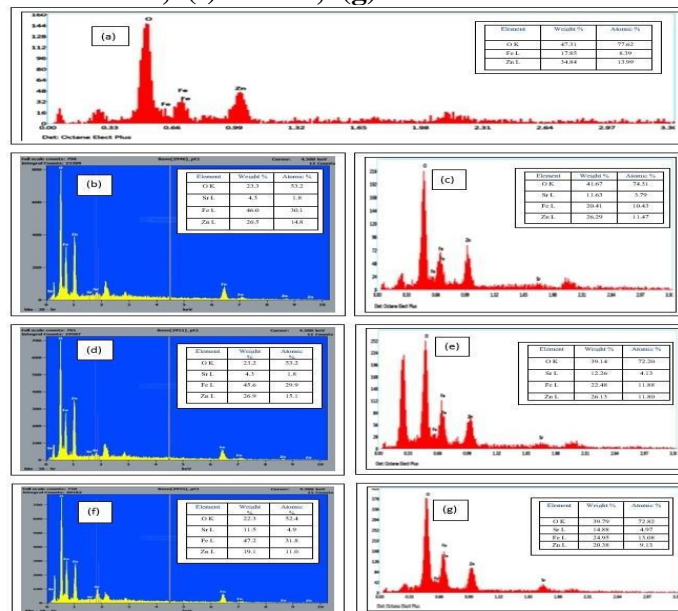


**Fig. 6: EDX image of  $Sr_xZn_{(1-x)}Fe_2O_4$  (a)  $x=0$ , (b)  $x=0.05$ , (c)  $x=0.10$ , (d)  $x=0.15$ , (e)  $x=0.20$ , (f)  $x=0.25$ , (g)  $x=0.30$**

**Evaluation with EDX**

Fig. 6(a-g) displays the EDX spectra of various compositions of Sr doped zinc ferrite nanomaterial. Elements O, Zn, and Fe can be seen in Fig. 6 (a), while Zn, Fe, O, and Sr can be seen in Fig. 6 (b)-(d). The spectrum shows no peaks attributable to other elements as impurities. No further spectral peaks attributable to individual elements are seen, proving that the chosen synthesis method is optimal. The stoichiometry of the produced compound is shown by the resulting fraction of these elements. The presence of oxygen in the substance suggests it could be employed as a humidity detector.

**Vibrating sample magnetometer (VSM) analysis:** The magnetic characteristics of the synthesized nanomaterial  $Sr_xZn_{1-x}Fe_2O_4$  ( $x=0.0, 0.05, 0.10, 0.15, 0.20, 0.25, 0.30$ ) were measured using a vibrating sample magnetometer at room temperature and a magnetic field range of -10 to +10 kOe. Hysteresis loop, also known as an M-H graph (magnetization vs magnetic field), is depicted in Figure 7.

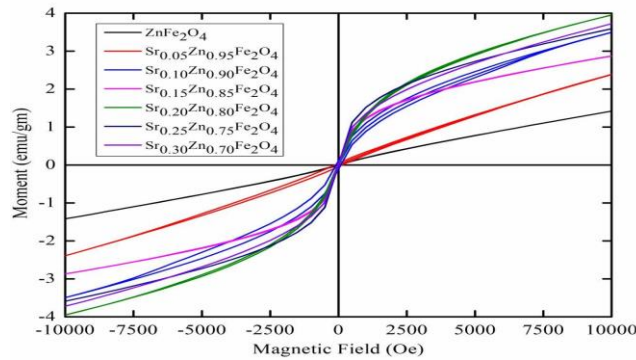


**Fig. 7: Hysteresis loop of Sr<sub>x</sub> Zn<sub>(1-x)</sub>Fe<sub>2</sub>O<sub>4</sub>**

The hysteresis pattern reveals the manufactured nanomaterial to be of soft magnetic character. In addition, the plot reveals that the saturation magnetization increases successively with the strontium content, with the exception of the composition x=0.20. Both the x=0.15 and x=0.25 compositions exhibit the superparamagnetic nature. The results of this plot's analysis may be found in Table 3.

**Table 3: Magnetic Parameters**

Sr concentration (x)	Saturation magnetization M <sub>s</sub> (emu/g)	Remanence M <sub>r</sub> (emu/g)	Coercivity H <sub>c</sub> (Oe)	Reduced remanence S = M <sub>r</sub> /M <sub>s</sub>
0.00	1.4208	0.01062	45.64	0.0075
0.05	2.3963	0.0453	139.37	0.0189
0.10	3.4843	0.1148	88.86	0.0329
0.15	2.8668	0.0137	7.47	0.0048
0.20	3.9547	0.0322	19.73	0.0081
0.25	3.6019	0.0179	7.96	0.0049
0.30	3.7195	0.0237	11.88	0.0064

**Evaluation with a Visible-Light Spectrometer**

The optical properties of the produced nanomaterials were evaluated in the range of 200 to 800 nm using a UV-Visible spectrometer (Model Baise UV-Visible spectrometer, Evaluation 201 Thermoscientific). The sample was examined for spectra at room temperature after being dissolved in citric acid solution and sonicated for 15 minutes. The peak absorption intensity was measured to be at 353 nm. A Tauc plot was generated from the captured absorbance spectra (Eg) to estimate the energy of the optical band gap. The Tauc connection is described as follows:

$$\alpha h\nu = A(h\nu - E_g)^n \dots\dots\dots(6)$$

where, n=1/2 for direct band gap, 2 for indirect bad gap

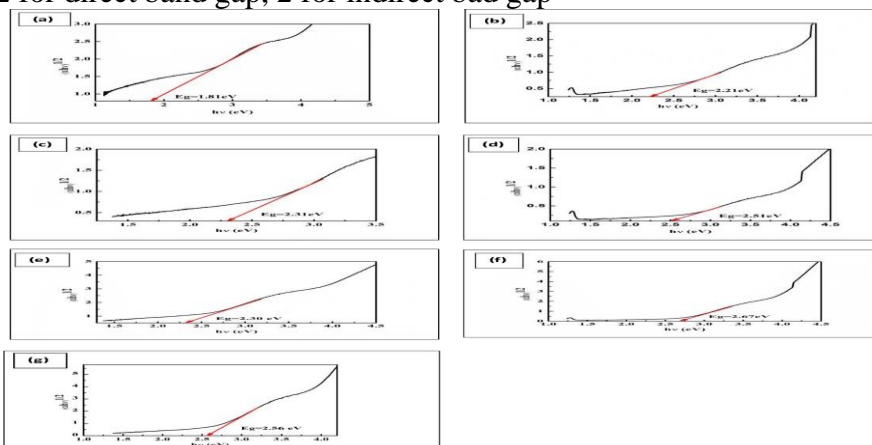


**Fig. 8: Tauc plot images of Sr<sub>x</sub> Zn (1- x)Fe<sub>2</sub>O<sub>4</sub>(a) x=0, (b) x=0.05, (c) x=0.10, (d) x=0.15, ( e)x=0.20, (f) x=0.25, (g) x=0.30**

The Tauc plot is shown in Figure 8. The x-intercept of this variation curve (E<sub>g</sub>) is how we calculate the band gap. Table 4 displays the computed band gap as a function of composition (x=0, 0.05, 0.10, 0.15, 0.20, 0.25, and 0.30).

**Table 4: Band gap values**

Compositions	Band Gap (eV)
ZnFe <sub>2</sub> O <sub>4</sub>	1.81
Sr <sub>0.05</sub> Zn <sub>0.95</sub> Fe <sub>2</sub> O <sub>4</sub>	2.21
Sr <sub>0.10</sub> Zn <sub>0.90</sub> Fe <sub>2</sub> O <sub>4</sub>	2.31
Sr <sub>0.15</sub> Zn <sub>0.85</sub> Fe <sub>2</sub> O <sub>4</sub>	2.51
Sr <sub>0.20</sub> Zn <sub>0.80</sub> Fe <sub>2</sub> O <sub>4</sub>	2.30
Sr <sub>0.25</sub> Zn <sub>0.75</sub> Fe <sub>2</sub> O <sub>4</sub>	2.67
Sr <sub>0.30</sub> Zn <sub>0.70</sub> Fe <sub>2</sub> O <sub>4</sub>	2.56

## MOISTURE SENSOR RESEARCH

### Humidity sensor characteristics

As shown in Fig. 2, the finished sensing element, complete with electrical connections, is stored in a humidity-controlled glass chamber. At room temperature and 100 Hz, the impedance (Z) of the thin film sensing element was determined for a range of 10-95% RH. In Fig. 9 we see the results of taking measurements of impedance (Z) at several levels of relative humidity (%RH). As can be shown in Fig.7, the impedance of zinc ferrite nanomaterial is improved with the doping of Sr atoms. The graph shows that the nature of the impedance change in pure and doped materials of different compositions is the same. A sensor's reaction is measured in terms of its sensitivity. Sensitivity to relative humidity is characterized mathematically as:

$$\text{Sensitivity} = \left| \frac{Z_1 - Z_2}{RH_1 - RH_2} \right| \dots\dots\dots(7)$$

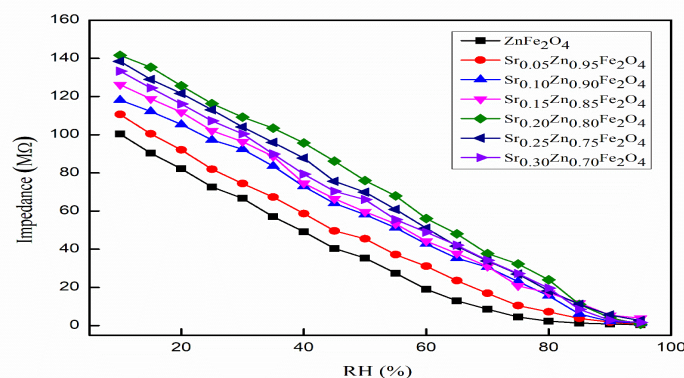


**Fig. 9: Variation of impedance with % RH of Sr<sub>x</sub>Zn<sub>(1-x)</sub>Fe<sub>2</sub>O<sub>4</sub> nanomaterials at 25 °C.**

**Reaction and Revitalization Times:** The response time of a humidity sensor is defined as the time required for the sensor to recover to 90% of its initial output following desorption or the time required for adsorption to reach its final output [Arunachalam et al., 2019, Tiwari et al., 2022]. According to the data presented in Fig.10, the response time was 19 s during the humidities' ascending order and 81 s during their descending order. The quick reaction and recovery times show that this humidity sensor is suitable for real-world use.

**Repetition:** The ability of a humidity sensor to reliably reproduce the same measurement under controlled conditions is an essential feature [Priya et al., 2021]. This quality demonstrates the sensing element's dependability. The designed humidity sensor in this investigation has a repeatability of 97.62 percent between 10 and 95.2 percent RH. Fig. 11 shows the repeatability curve. The great repeatability of the manufactured humidity sensor is indicative of its usefulness.

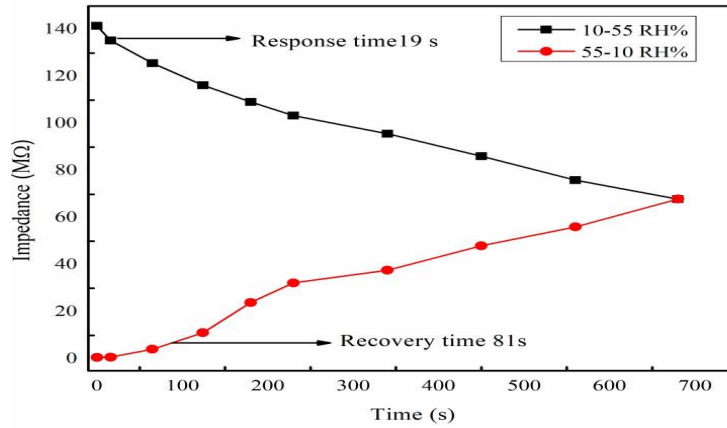
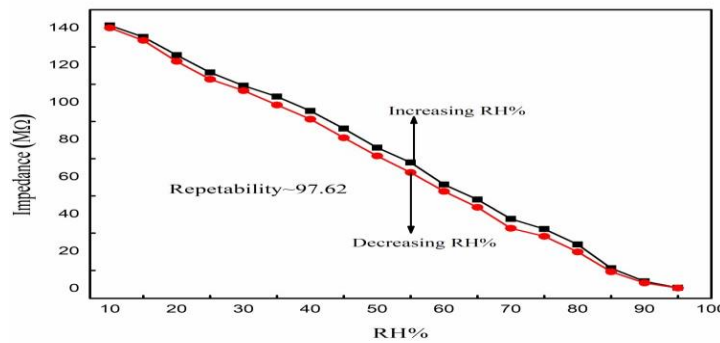


**Figure 10: The Response and Recovery time curve for  $Sr_x Zn_{(1-x)}Fe_2O_4$  (for  $x=0.2$ ) at**

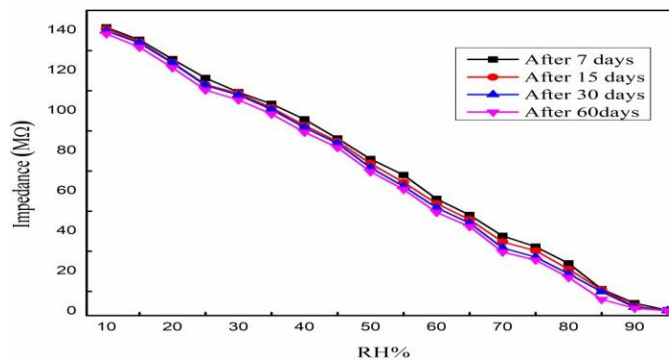


25°C.

**Fig. 11. The repeatability curves of  $Sr_x Zn_{(1-x)}Fe_2O_4$  (for  $x=0.2$ ) nanomaterials at 25 °C**

### AGING EFFECT

An important characteristic of a sensor, the aging effect exposes the long-term durability of the sensor's detecting element. It is often checked again after 7 or 15 days. After 15 days, 60 days,



and at different degrees of humidity, this study looked at the aging effect test. **The Stability curves of  $Sr_x Zn_{(1-x)}Fe_2O_4$  (for  $x=0.2$ ) nanomaterials at 25 °C.**

## CONCLUSION

Sol-gel self-ignition was used to create strontium-doped nano zinc ferrites. Nanoparticles produced using PXRD, FTIR, FESEM, EDX, VSM, and UV-Visible methods were characterized. Nanoparticles made using this method exhibit a cubic spinel ferrite phase with space group  $Fd\bar{3}m$ , as seen in their XRD patterns. Crystallite size decreases from 50.32 nm to 28.33 nm after strontium doping, and the lattice constant increases from 8.442 to 8.449. Water ( $1624\text{ cm}^{-1}$ ) and a hydroxyl group ( $3416\text{ cm}^{-1}$ ) can be seen in the infrared spectra of the produced sample. As a thin film humidity sensor,  $\text{Sr}_{0.2}\text{Zn}_{0.8}\text{Fe}_2\text{O}_4$  nanoparticles were investigated, with an average sensitivity of 1.918 M/%RH. The response time was 19 seconds and the recovery time was 81 seconds at room temperature.

## REFERENCES

1. F. Brisse, R. Lecoq, N. Millot, and H. Randrianantoandro, "Magnetic, optical and catalytic properties of transition metal-substituted zinc ferrite nanoparticles synthesized by a sol-gel method," *Materials Chemistry and Physics*, vol. 112, no. 3, pp. 934-940, 2008.
2. P. S. Aruna, G. Venkateswarlu, A. Hymavathi, C. Ravikumar, and R. P. Vijayalakshmi, "Structural, magnetic and dielectric properties of strontium substituted zinc ferrites," *Materials Research Express*, vol. 6, no. 10, 2019.
3. S. B. Kale and S. E. Shirsath, "Enhanced magnetic properties of Sr-doped  $\text{ZnFe}_2\text{O}_4$  ferrite nanoparticles synthesized by sol-gel auto-combustion method," *Journal of Alloys and Compounds*, vol. 650, pp. 325-331, 2015.
4. G. K. Bichile, P. R. Jadhav, and S. S. Jadhav, "Synthesis, characterization and dielectric properties of strontium doped zinc ferrite nanoparticles," *Materials Science and Engineering: B*, vol. 179, no. 9, pp. 68-75, 2014.
5. M. Gabal, H. M. El-Sayed, and E. M. El-Sherbini, "Strontium substitution in zinc ferrite prepared by co-precipitation and its effect on the microstructure and magnetic properties," *Materials Chemistry and Physics*, vol. 140, no. 2-3, pp. 214-222, 2013.
6. G. C. Pimentel, M. S. S. da Silva, A. L. L. Pimentel, M. M. Oliveira, and E. R. Neiva, "Synthesis and characterization of strontium-doped zinc ferrite nanoparticles for photocatalytic applications," *Ceramics International*, vol. 45, no. 17, pp. 21458-21465, 2019.
7. P. S. Aruna, A. Hymavathi, C. Ravikumar, R. P. Vijayalakshmi, and G. Venkateswarlu, "Magnetic and dielectric properties of strontium substituted zinc ferrite nanoparticles," *Journal of Magnetism and Magnetic Materials*, vol. 491, pp. 165488, 2019.
8. R. J. Choudhary, A. Sen, P. A. Alvi, K. Asokan, and S. B. Ogale, "Effect of Sr doping on magnetic and electronic properties of  $\text{ZnFe}_2\text{O}_4$  nanoparticles," *Journal of Applied Physics*, vol. 107, no. 09E126, 2010.
9. M. R. Karim, S. B. Qadri, J. S. Horwitz, and D. B. Chrisey, "Strontium-doped zinc ferrite thin films prepared by pulsed laser deposition," *Journal of Applied Physics*, vol. 87, no. 9, pp. 4818-4823, 2000.
10. L. X. Nghia, T. A. Tuan, T. D. Hien, D. D. Dung, and V. D. Lam, "Magnetic and dielectric properties of strontium-doped zinc ferrite nanoparticles synthesized by the co-precipitation method," *Journal of Magnetism and Magnetic Materials*, vol. 476, pp. 254-258, 2019.
11. M. Gabal, A. H. Bhrawy, and E. R. Shaaban, "Structural and magnetic properties of  $\text{ZnFe}_{2-x}\text{Sr}_x\text{O}_4$  nanoparticles synthesized by the citrate precursor method," *Journal of Alloys and Compounds*, vol. 503, no. 1, pp. 30-37, 2010.
12. M. A. Mallick, M. Pal, M. N. Sinha, A. Banerjee, S. R. Bhattacharya, and S. K. Sen, "Effect of  $\text{Sr}^{2+}$  substitution on the structure and magnetization behavior of nanosized  $\text{ZnFe}_2\text{O}_4$ ," *Journal of Magnetism and Magnetic Materials*, vol. 312, no. 1, pp. 210-217, 2007.